IEEE Photonics Journal
An IEEE Photonics Society Publication

Open Access

Characterization of Evanescent Field Gas Sensor Structures Based on Silicon Photonics

Volume 10, Number 5, September 2018

Christian Ranacher
Cristina Consani
Natalie Vollert
Andreas Tortschanoff
Markus Bergmeister
Thomas Grille
Bernhard Jakoby

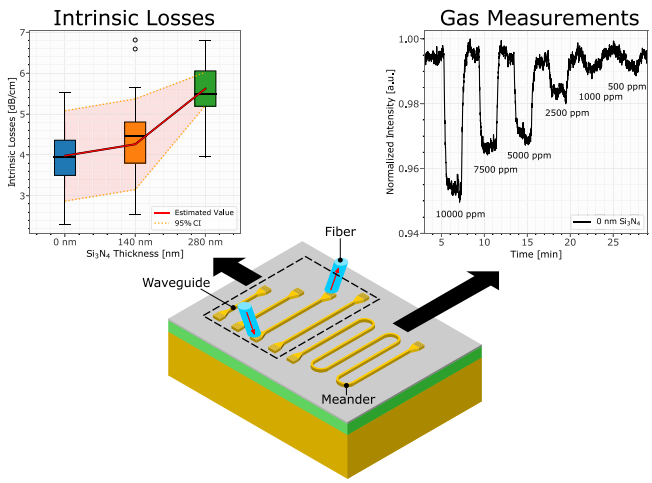

DOI: 10.1109/JPHOT.2018.2866628
1943-0655

Characterization of Evanescent Field Gas Sensor Structures Based on Silicon Photonics

Christian Ranacher,[1] **Cristina Consani**,[1] **Natalie Vollert**,[1] **Andreas Tortschanoff**,[1] **Markus Bergmeister**,[2] **Thomas Grille**,[2] **and Bernhard Jakoby**[3]

[1]Carinthian Tech Research AG, Villach 9524, Austria
[2]Infineon Technologies Austria AG, Villach 9500, Austria
[3]Institute for Microelectronics and Microsensors, Johannes Kepler University Linz, Linz 4040, Austria

DOI:10.1109/JPHOT.2018.2866628

Manuscript received April 20, 2018; revised August 6, 2018; accepted August 18, 2018. Date of publication August 23, 2018; date of current version September 11, 2018. This work was performed within the Competence Centre "ASSIC Austrian Smart Systems Integration Research Center" and "LCM Linz Centre of Mechatronics," which was supported in part by the Federal Ministries of Transport, Innovation and Technology (BMVIT) and Digital and Economic Affairs (BMDW) and in part by the Federal Provinces of Carinthia, Styria, and Upper Austria within the COMET—Competence Centers for Excellent Technologies Programme. Corresponding author: Christian Ranacher (e-mail: christian.ranacher@ctr.at).

Abstract: Photonic sensors that operate in the mid-infrared spectral range are an emerging field for photonic microsystems. In this paper, we present a photonic gas sensor concept based on silicon waveguides using infrared evanescent field absorption. The waveguides were specifically designed for CO_2 sensing at a wavelength of $\lambda = 4.26\,\mu$m as possible application for the proposed sensor platform. The waveguide cross section as well as the substructure were investigated using finite-element simulations and the devised structures were fabricated using mass fabrication processes exclusively. In order to evaluate the potential for long interaction path lengths using polysilicon strip waveguides, a study on the intrinsic losses of polysilicon waveguides was conducted. The lowest intrinsic damping that was obtained for polysilicon strip waveguides was 3.98 dB/cm. Furthermore, the sensing capability of the devised waveguides was tested with quantitative CO_2 measurements down to a concentration of 500 ppm CO_2. From the quantitative measurements, the evanescent field ratio was estimated and was in the range between $\eta = 14\%$–16%.

Index Terms: Optical gas sensing, integrated silicon photonics, silicon waveguide, evanescent field absorption, intrinsic losses.

1. Introduction

Gas sensing for air quality monitoring is an emerging application field for photonic microsystems. Air quality is a significant factor for public health and therefore, there is great interest in small and cost-efficient sensors for the monitoring of environmental gases, which could be integrated in mobile devices and used especially in urban areas and in confined spaces such as buildings. In this work we present a study on silicon waveguides which could be used as active structures for integrated and miniaturized gas sensors based on evanescent field absorption. This approach stands in contrast to metal oxide gas sensors, see, e.g., [1], which are a frequently proposed

approach for miniaturized CMOS compatible microsensors for gas sensing. The physical principle of the presented sensor is evanescent field infrared absorption using a silicon waveguide.

The investigated structures are poly-silicon strip waveguides in which an electromagnetic (EM) mode is excited using an external infrared source. The silicon waveguide is a dielectric waveguide, which features a significant energetic portion of the mode propagating outside of the waveguide core, if the cross-section dimensions are designed accordingly. The part of the mode that propagates outside the waveguide in the so called cladding region, is referred to as evanescent field and decays exponentially with the distance from the waveguide. Detailed descriptions of the theoretical concepts that are behind the mentioned mechanisms can be found, e.g., in [2]–[4]. If an absorbing medium is located in the vicinity of the waveguide, the evanescent field is absorbed and the total modal power decreases as the mode propagates along the waveguide, which is detected in terms of a reduced transmitted intensity.

Evanescent field absorption gas sensing is a well recognized approach, for example in evanescent fiber optics applications (discussed, e.g., in [5]). In order to use this concept for CMOS integrated devices in the mid-infrared, there are major issues to overcome, which are particularly related to the optical properties of the materials in the mid-infrared range and their compatibility to industrial CMOS technology [6], [7]. Such obstacles are significant intrinsic losses of the materials, as well as the lack of suitable radiation sources and detectors. An integrated optical gas sensor consists of at least a source, an interaction path of the gas with the radiation and a detector. In this work we focused on the investigation of evanescent field absorption gas sensor structures based on silicon strip waveguides as potential platform for gas sensors. Within this study, two important parameters, the intrinsic losses and the evanescent field ratio, which determines the part of the EM mode that propagates in the gas region, were investigated. The structures were optimized for CO_2 sensing, which is one of numerous applications. Therefore the structures were designed for the wavelength region of the CO_2 absorption band in the mid-infrared which is centered around 4.26 μm. In literature, several studies have been presented that numerically investigated evanescent field sensing in the CO_2 absorption region based on silicon photonics. An example is [8] where silicon on sapphire waveguides for CO_2 sensing were numerically investigated. Another example is the numerical study on photonic crystal ring resonators for CO_2 sensing [9]. The authors of [10] and [11] presented a concept for an evanescent field gas sensor based on free standing silicon waveguides, with the emphasis on design and fabrication. Still, experimental studies of waveguides that operate in the mid-infrared region around 4.26 μm are rare.

In this work we present an experimental characterization of silicon strip waveguides which can be mass-produced with standard CMOS processes. In section 2 we explain the design and modeling of those waveguide structures in detail, and in section 3 we describe the experimental fabrication as well as the set-up that was used for the optical characterization. In section 4 we present the experimental results on the intrinsic losses, including thorough mathematical analysis concerning the statistical significance of the results, and furthermore results on the evanescent field ratio.

2. Modeling and Design

2.1 Concept

Sensing of CO_2 represents a typical application for optical IR-based gas sensing. Therefore the strip waveguide structures were designed for the center wavelength of the CO_2 absorption band in the mid-infrared, i.e. 4.26 μm. The devised waveguides were characterized using an external mid-infrared source and an external infrared detector. In order to couple the radiation into and out of the waveguide, a taper as well as a launchpad with a diffraction grating were added at both ends of the waveguide. The dimensions of the grating coupler were adopted from previous work [12]. Since these coupling structures are only a preliminary means to couple from an external source and to an external detector (the ultimate goal is to develop a fully integrated sensor), respectively, it is not further discussed within this work.

In order to investigate the intrinsic losses, a method that is related to the cutback method [13] was used and is described in more detail in section 4–1. For this experiment, four strip waveguides with

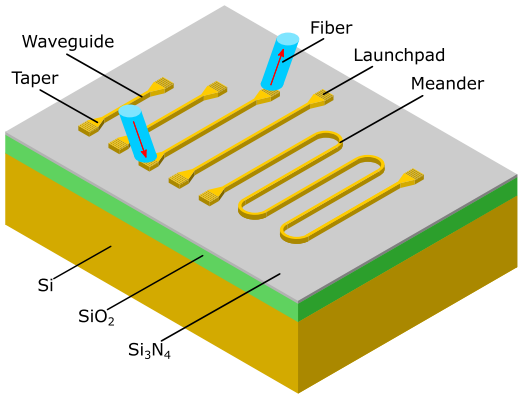

Fig. 1. Schematic representation of the sensor test structure chip. The test structures comprise strip waveguides of various lengths for the characterization of the intrinsic losses, as well as a strip waveguide in the shape of a meander for the gas measurements.

different lengths of 5.0 mm, 7.5 mm, 10.0 mm and 12.5 mm were used. In order to test the concept for gas sensing, and for the determination of the evanescent field ratio, a strip waveguide meander with a length of 2.0 cm and loop radii of 25 μm was used. Fig. 1 shows a schematic representation of the strip waveguide structures.

The sensor structures are fabricated using processes that are used for MEMS mass production exclusively, which leads to certain design restrictions that needed to be taken into account. One limitation is the process for the deposition of the waveguide layer (poly silicon) which restricted the height of the Si waveguide to 660 nm. The waveguide width was optimized using a FEM model and furthermore different configurations for the substructure were numerically investigated. Similar structures have already been investigated by our group using simple slab waveguides and strip waveguides located on a suspended Si_3N_4 membrane [14], [15]. In the present work a solid substructure was used and different layer configurations were compared. The waveguides reside on a silicon substrate covered by a layer of 2000 nm SiO_2, which was chosen sufficiently thick to avoid significant leakage of the guided mode into the substrate, and, for some of the configurations, a layer of Si_3N_4 with varying thicknesses. The introduction of a Si_3N_4 layer between the waveguide and the oxide serves two reasons. There is a significant discrepancy in the optical parameters that can be found in literature and our goal was to investigate the influence of Si_3N_4 on the intrinsic losses. Furthermore, when integrating the IR source and detector it might be necessary to thermally decouple both elements from the substrate. This could be achieved by using a thin membrane fabricated of Si_3N_4, which is preferable over SiO_2 due to its high mechanical stability. Therefore we also investigate the compatibility of Si_3N_4 for the proposed sensing platform.

2.2 Modeling of the Strip Waveguide

A model of the strip waveguide together with its substructure was developed using the finite element method software COMSOL Multiphysics 5.3a. The model was used to optimize the dimensions of the waveguide and to investigate the effect of the intermediate Si_3N_4 layer on the mode properties. The optical material parameters for Si and SiO_2 were obtained from literature (Si [16] and SiO_2 [17]). Concerning Si_3N_4, there is a big discrepancy in literature since its optical characteristics strongly depend on the fabrication process. The material parameters for Si_3N_4 were taken from [18] where Si_3N_4 thin films were prepared using the same fabrication method as in our work. For the simulations only the real part of the refractive index n' was considered, because due to the low absorption coefficient of the used materials in the considered wavelength range, there is no accurate data for the extinction coefficients n'', i.e. the imaginary part of the refractive index. Using the wave optics module of COMSOL Multiphysics, a modal analysis was conducted for the cross-section of

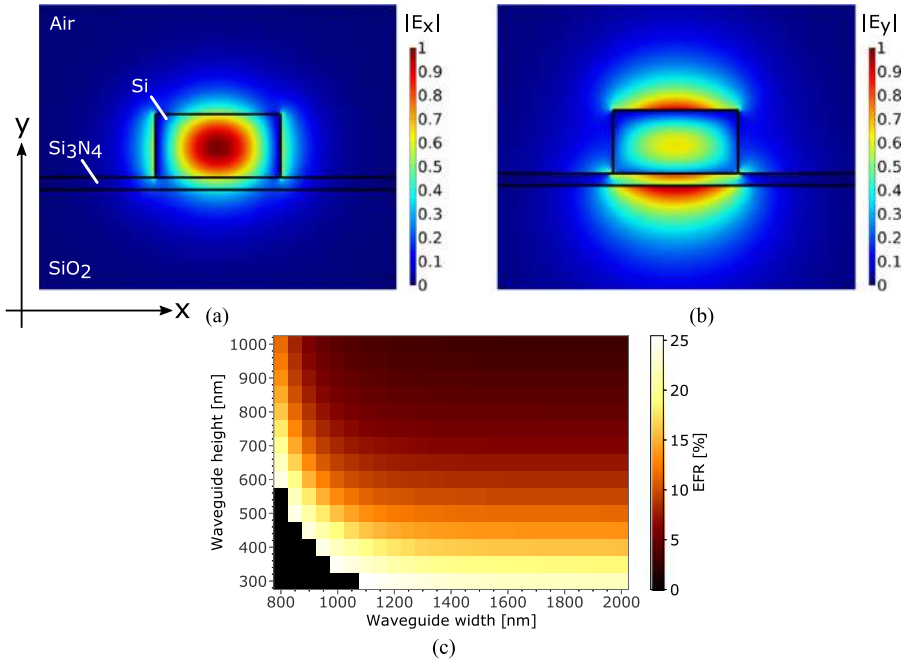

Fig. 2. (a–b) Field distribution of the modes that were investigated by FEM simulations. The plots show results for the configuration with 140 nm Si_3N_4. The plots show the field distribution of $|E_x|$ for the fundamental quasi-TE mode (a) and the field distribution of $|E_y|$ for the fundamental quasi-TM mode (b).(c) A color map depicting the evanescent field ratio for the quasi-TE mode as function of the waveguide width and height. The plot shows the results for the configuration without Si_3N_4.

the waveguide configuration. Qualitative simulation results are shown for a Si_3N_4 layer thickness of 140 nm in Fig. 2a–b. The plots show the normalized electric field distribution of the dominant transverse electric field components $|E_x|$ and $|E_y|$, for the fundamental quasi-TE mode (a) and the fundamental quasi-TM mode (b), respectively. The waveguide cross section of the silicon strip waveguide is indicated by the small rectangle in the middle. The Si_3N_4 layer below the waveguide is indicated by the two horizontal lines. The area below the Si_3N_4 layer is SiO_2 and the area on top of the Si_3N_4 layer, except for the waveguide, is air. The simulations were carried out using a domain size that was much bigger than the domain shown in Fig. 3 to avoid spurious effects at the boundary of the simulation domain. In the actual simulation domain also the silicon substrate below the SiO_2 was taken into account. Due to the electric displacement continuity condition ($\epsilon_1 \cdot \vec{E}_1 \cdot \vec{n} = \epsilon_2 \cdot \vec{E}_2 \cdot \vec{n}$) the surface normal component of the electric field shows a distinct discontinuity on the side walls for the quasi-TE mode and on top and the bottom for the quasi-TM mode.

The quantitative results obtained from the simulations are the real part of the effective mode index n'_{eff} and the evanescent field ratio η, defined below, which was investigated for various waveguide dimensions and for various Si_3N_4 layer configurations. The condition for guided modes is [2]

$$n'_{waveguide} > n'_{eff} > n'_{cladding}. \tag{1}$$

If the condition is not fulfilled i.e. n'_{eff} is smaller than $n'_{cladding}$, the mode is unguided (sometimes these modes are also referred to as leaky or improper modes). This means that the EM field is oscillatory and not exponentially decaying (evanescent) in the region outside of the strip, which leads to an EM field that leaks out into a radiation mode [2]. The evanescent field ratio (EFR) η is defined as the ratio of the transmitted power in the gas/air part to the total modal power [8]:

$$\eta = \frac{\int\int_{Gas} \vec{S} \cdot \vec{n}\, dxdy}{\int\int_{All} \vec{S} \cdot \vec{n}\, dxdy} \tag{2}$$

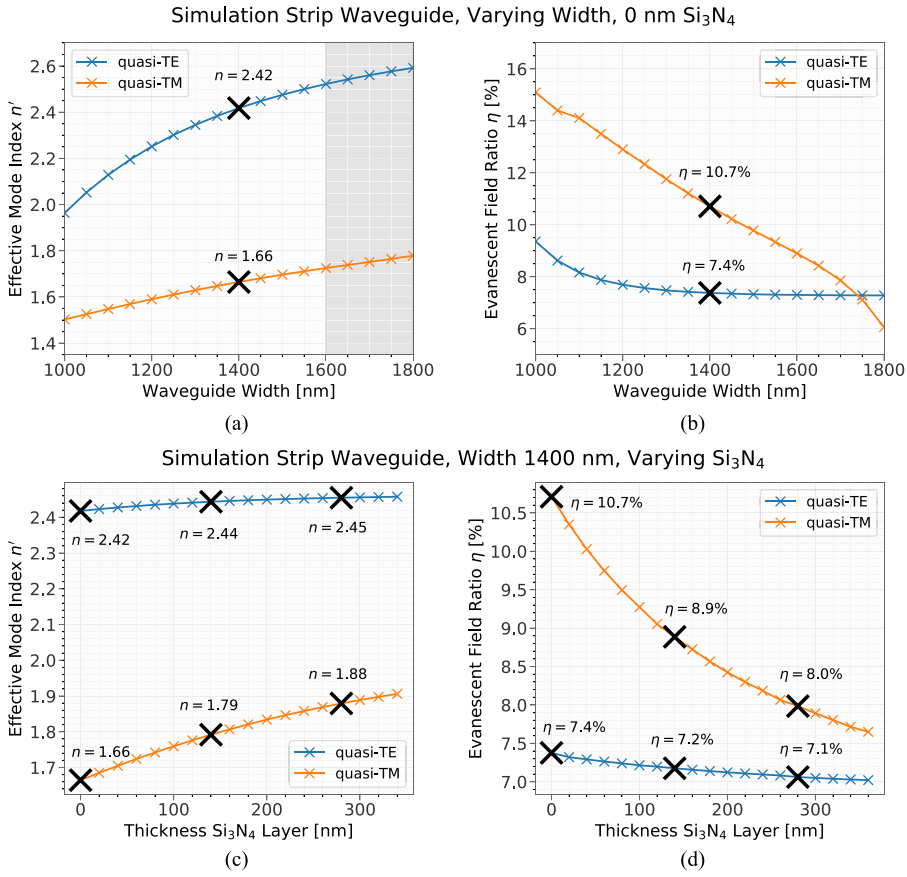

Fig. 3. Results from the FEM simulations for a waveguide height of 660 nm. The plots (a) and (b) show the real part of the effective mode index n' and the evanescent field ratio, respectively, as a function of the strip waveguide width. The shaded area in (a) indicates the area where also a higher order quasi-TE mode is guided. The plots (c) and (d) show the real part of the effective mode index n' and the evanescent field ratio, respectively, as a function of the Si_3N_4 layer thickness. The points which are marked by the big crosses are of special interest since these are the waveguide width/Si_3N_4 layer thicknesses which were investigated experimentally.

Here $\vec{S}$ denotes the Poynting vector and $\vec{n}$ the unit vector orthogonal to the waveguide cross-section, which is the z direction in the present case. The EFR is a measure for the fraction of the EM field that interacts with a surrounding gas and thus it is closely related to the sensitivity of the waveguide when it is used as absorption sensor.

Exemplary, the EFR of the fundamental quasi-TE mode is plotted in Fig. 2c for various waveguide dimensions (configuration without Si_3N_4). The waveguide behaves as expected showing a higher EFR for small waveguide dimensions, due to less confinement of the mode in the waveguide core. Nevertheless, intrinsic losses due to absorption in the lossy cladding or leakage due to the surface roughness will increase with smaller dimensions as the mode is less confined in the core. Furthermore, if the dimensions get too small no guided mode can propagate, which is indicated by the dark area in the bottom left corner in Fig. 2c. As mentioned before, the height of the waveguide was restricted to 660 nm, in order to be compatible with our standard deposition process. The waveguide with the height fixed to 660 nm was investigated in more detail below.

The simulation results using a waveguide height of 660 nm are depicted in Fig. 3. Fig. 3a shows the effective mode index for various waveguide widths using a substructure configuration without Si_3N_4. According to Eq. (1) both fundamental modes are guided for the whole range that was investigated, since $n'_{SiO2} = 1.38$ @ $\lambda = 4.26\,\mu$m [17]. The shaded area indicates where also a higher

TE-mode is guided. In order to avoid multiple guided TE modes (for widths higher than 1600 nm) but allowing highest possible power transmission with a sufficient EFR, a waveguide width of 1400 nm was chosen. Furthermore, since a larger fraction of the mode is confined in the waveguide core (compared to smaller widths), it might also help to reduce losses which are caused by the roughness of the sidewalls. The waveguide dimensions are thus 1400 nm in width and 660 nm in height. Similar dimensions have also been used in [19], where a silicon platform for broad-band infrared photonics was investigated. In order to find the best trade-off between high evanescent field ratio and low intrinsic losses, a systematic experimental study would be necessary. The EFR was evaluated according to Eq. (2) and is plotted in Fig. 3b, leading to evanescent field ratios of 7.4 % for the quasi-TE mode and 10.4 % for the quasi-TM mode (for the experimentally investigated waveguide dimension).

Using the devised design parameters for the waveguide dimensions, the influence of an Si_3N_4 intermediate layer between Si and SiO_2 was investigated. The effective mode indices and the evanescent field ratios are plotted in Fig. 3c-d. The layer thickness of Si_3N_4 showed an impact on the effective mode index, where in both cases the effective mode index increased with the Si_3N_4 layer thickness. According to the simulation results the condition for guided modes is fulfilled for the quasi-TE mode, for all of the investigated Si_3N_4 layer thicknesses (see Fig. 3; the refractive indices of the cladding materials are $n'_{Si3N4} = 1.88$ @ $\lambda = 4.26\,\mu$m [18], $n'_{SiO2} = 1.38$ @ $\lambda = 4.26\,\mu$m [17] and $n'_{Air} = 1$). For the quasi-TM mode, the determined lower effective mode index is related to the fact that the quasi-TM mode is guided in the silicon waveguide as well as in the Si_3N_4 layer (for configurations with Si_3N_4) and is only evanescent in the SiO_2 and air regions.

The EFR for the quasi-TE mode ranges from 7.4 % for 0 nm Si_3N_4 thickness to 7.1 % for 280 nm. As indicated by the field distribution in Fig. 2a-b, the EFR of the quasi-TM mode is higher and ranges from 10.7 % for 0 nm Si_3N_4 thickness to 8.0 % for 280 nm. Since a larger portion of the quasi-TM mode propagates in the lossy cladding material compared to the quasi-TE mode, the quasi-TM mode will also have higher intrinsic losses. The field enhancement on the sidewalls and on the top and bottom of the waveguide, respectively, is particularly beneficial as it increases the evanescent field ratio.

3. Experimental

3.1 Fabrication of the Sensor

The devised structures were fabricated on eight inch Si wafers, using established semiconductor mass production processes such as chemical vapor deposition, lithography and dry etching. A silicon oxide layer with a thickness of 2 μm was deposited on the silicon substrate via low pressure chemical vapor deposition (LPCVD) at a temperature of 670 °C. Si_3N_4 layers with different thicknesses were deposited on the oxide layer by LPCVD at a temperature of 780 °C. Due to the high temperature during deposition, hydrogen bonds in the layer were avoided and a subsequent annealing step was not necessary. On top of the Si_3N_4 layer an amorphous silicon layer was deposited using LPCVD and annealed at 700 °C for 30 s to achieve a poly-crystalline silicon layer. Eventually, the devised waveguide structures were etched into the poly-crystalline silicon via two dry etching processes (waveguide and grating).

3.2 Measurement Setup

The topography of the fabricated waveguides was investigated using a Hitachi S4800 scanning electron microscope. The surface roughness of the Si structures and the SiO_2/Si_3N_4 layer, as well as the topography of the strip waveguides was investigated with an atomic force microscope (AFSEM, GETec). No metal layer was deposited on the samples prior to the investigation in order to preserve the original nanostructure of the samples. Therefore it was necessary to use a low acceleration voltage of 2 kV for the scanning electron microscopy to avoid charging effects of the surface.

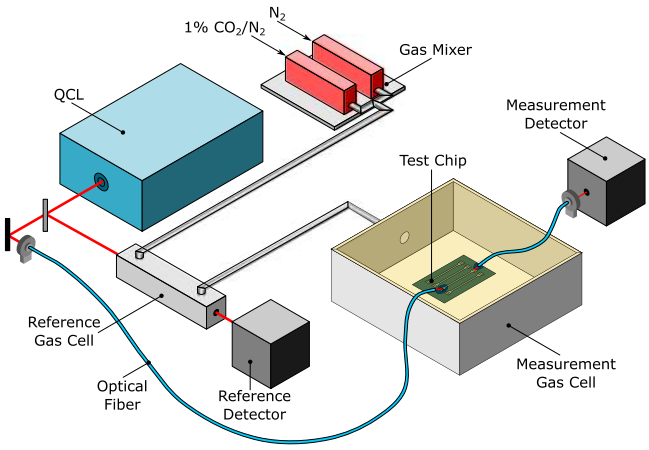

Fig. 4. Schematic representation of the measurement setup. The dimensions of the individual parts do not represent the reality.

The characterization of the intrinsic losses as well as the gas measurements were carried out using a custom test-bench which is shown schematically in Fig. 4. The test-bench comprises a quantum cascade laser (QCL) as mid-infrared radiation source, optical fibers, a stage for placing the test chips, IR detectors, a reference transmission cell and a custom gas mixer.

The used quantum cascade laser was a MIRcat laser system from Daylight Solutions and was operated in pulsed mode. The radiation of the QCL was split into a reference and a measurement beam using a beam splitter. The reference beam passed through a custom-made transmission gas cell with a length of 10 cm before hitting a thermoelectrically cooled MCT detector from Vigo Systems (PVI-2TE-6). The measurement beam was guided onto the sensor and from the sensor to the measurement detector (Vigo Systems PVI-2TE-6) via optical fibers (Thorlabs MF11 and and MZ41L1). The core diameter of the fibers was 100 μm and 450 μm, respectively. The signal readout was performed with a lock-in amplifier (Princeton Instruments). While the characterization of the intrinsic losses was carried out on wafer-level, the gas measurements were carried out on single chips. The single test chips were placed in a 3D printed gas cell (acrylate-type plastic), as indicated in Fig. 4. The gas cell comprised a gas inlet and a holder for the test chip. The top of the cell was only partially covered, and therefore not sealed. The cover of the cell had openings for the fibers to enter the cell, which, at the same time served as outlets for the gas, in order to keep the chamber virtually at ambient pressure. During the gas measurements the cell was flushed with CO_2/N_2 mixtures at a total flow rate of 100 ml/min using a custom gas mixer that consists of two mass flow controllers (red-y, smart controller GSC). For the quantitative CO_2/N_2 measurements an integration time of 300 ms was used at the lock-in amplifier.

4. Results and Discussion

Prior to the optical characterization the topography of the fabricated structures was investigated and the results are shown in Fig. 5.

The SEM images show a part of a strip waveguide as well as a loop of the meander showing the quality of the fabrication process. As visible in Fig. 5, the sidewalls are significantly rougher than the top surfaces which is a result of the dry-etching process. It is crucial to achieve smooth surfaces since the surface roughness has a big impact on the intrinsic damping, due to out-scattering effects. The AFM measurements revealed that the surface roughness is considered to be sufficiently low. The root mean square height of a surface (S_q) was evaluated on the top of the Si layer as well as on the SiO_2 and the Si_3N_4 layer, respectively, and was $S_q \approx 1$ nm for all measurements. Although the measured surface roughness was virtually equal for all layers, the measured morphology showed

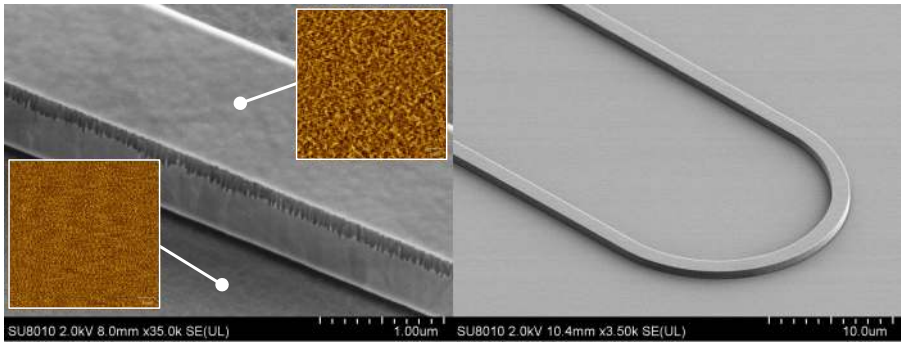

(a) (b)

Fig. 5. (a) SEM analysis of the strip waveguide. The insets show AFM measurements to compare the surface roughness of the waveguide (poly-Si) and the top layer of the supporting structure (SiO_2 for the depicted measurement). The insets correspond to an area of 28 μm · 28 μm and the pointers only indicate to which layer the AFM measurements should be assigned and do not indicate the actual measurement position. (b) SEM image taken from a loop of the meander structure.

bigger structures on the silicon surfaces, which is indicated in the insets in Fig. 5a. This may indicate individual Si-crystals as the deposited material is poly-Si. The height of the strip waveguide was measured for all configurations using the AFM and was 623 nm (0 nm Si_3N_4), 586 nm (140 nm Si_3N_4) and 585 nm (280 nm Si_3N_4), which is a deviation from the designed 660 nm. This will lead to a minor modification of the effective mode index and the evanescent field ratio that was obtained from simulation.

An adapted Beer-Lambert law was used to model the power that is transmitted through the strip waveguide:

$$I = I_0 \cdot e^{-a_c - \alpha_0 \cdot z} \cdot e^{-\eta \cdot c \cdot \epsilon \cdot z} \tag{3}$$

I denotes the measured transmitted intensity and I_0 the initial intensity. The first exponential describes the coupling losses characterized by a parameter a_c, and the intrinsic losses characterized by a parameter α_0 in dependence of the length of the individual waveguide z. The second exponential describes the attenuation of the transmitted power due to the evanescent field absorption caused by a surrounding medium, with the evanescent field ratio η, the absorption coefficient ϵ and the interaction length z, which is the length of the waveguide in the present case. The two crucial parameters of the waveguide for sensing applications, the intrinsic losses and evanescent field ratio, are determined in the following sections.

4.1 Characterization of Intrinsic Losses

The aim of this experiment was to characterize the intrinsic losses of the devised strip waveguide and to determine the influence of the Si_3N_4 layer. As already described, due to the lack of reliable literature data for the extinction coefficients of the used materials, an empirical approach is necessary. The intrinsic losses were evaluated for three configurations, were the thickness of the Si_3N_4 layer was varied. The Si_3N_4 was part of the substructure that consisted of the silicon substrate, a 2 μm SiO_2 layer and on top a Si_3N_4 layer with thicknesses of 0 nm, 140 nm and 280 nm (see also scheme in Fig. 1).

The intrinsic losses were determined using an approach that is related to the cutback method. Four strip waveguides with different lengths (5.0 mm, 7.5 mm, 10.0 mm and 12.5 mm) were used and the transmitted IR radiation was measured. During the experiment, the QCL was tuned to 4.17 μm which is outside the CO_2 absorption band in order to avoid an influence of the ambient CO_2 concentration. The fibers were approached to the grating couplers and the lateral position was manually adjusted in order to achieve the maximum intensity at the detector. Since the transmitted

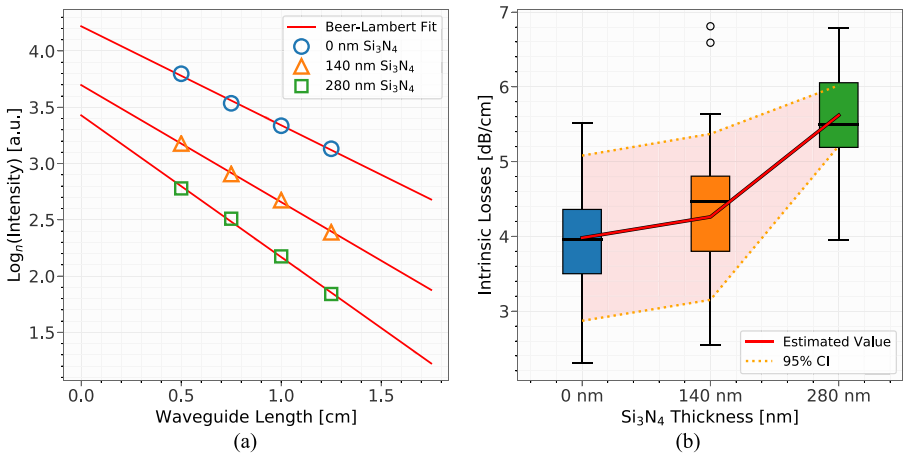

Fig. 6. (a) The plot shows representative measurement results of each configuration together with the Beer-Lambert fit. (b) Boxplots of the fitted data together with estimated means and their 95% confidence interval obtained from the ANOVA analysis.

intensity is highly sensitive to the fiber position, the measurement is challenging and offers great potential for uncertainties. In order to improve the statistic significance of the obtained results, a total of 81 measurements were conducted. For each configuration (0 nm, 140 nm and 280 nm Si_3N_4 layer thickness), three chips were measured on three different wafers, with three replicates per chip measurement. For every measurement the maximum transmitted intensities through the four waveguides with different lengths were recorded. Results from representative measurements are plotted in Fig. 6a, showing the natural logarithm of the recorded intensities.

The recorded intensities were fitted using the first part of the Beer-Lambert law (Eq. 3) in the form of:

$$I = I_0 \cdot e^{-a_c} \cdot e^{-\alpha_0 \cdot z} = \kappa \cdot e^{-\alpha_0 \cdot z} \tag{4}$$

Here I denotes the measured transmitted intensity, κ an arbitrary fit parameter that comprises the two unknown parameters, i.e. the initial intensity I_0 and the coupling losses a_c. Futhermore z denotes the length of the waveguide and α_0 the intrinsic loss. The latter is the parameter of interest. The two fit parameters were fitted using a least squares algorithm. The fits are also shown in logarithmic form in Fig. 6a. Besides different slopes, which can be assigned to the intrinsic loss α_0, also the fit parameter κ differs, which can be assigned to different coupling efficiencies. The fit parameter κ showed a variability for measurements on different chips, in particular between measurements on chips of different configurations. The κ for measurements within one chip was assumed to be constant. The intrinsic losses that were obtained for each replicate of the measurements are shown in Fig. 6b as box plots. The boxes represent the quartiles of the data, the black horizontal line in the middle of the box represents the median of the data and the whiskers are the most extreme data points ignoring outliers, which are shown as the fliers.

The box plot already gives a first clue about a possible influence of the Si_3N_4 layer thickness on the intrinsic losses, but these values may be also affected by other sources of variation, e.g., the wafer or chip measured. So, in order to determine if there is an actual significant difference for the individual configurations (i.e. the Si_3N_4 layer thickness) an ANOVA (ANalysis Of Variance) has been performed [20]. This method is mostly used to compare group means in order to confirm or disprove a potential effect of different treatments, while also accounting for influences of other variables. Here, the ANOVA model has the following form

$$y_{ij} = \mu + \alpha_i + \beta_{j(i)} + \varepsilon_{ij}, \tag{5}$$

TABLE 1
Estimated Mean Effect of the Three Different Si_3N_4 Layer Thicknesses and Corresponding 95% Confidence Intervals

Si_3N_4	Estimate [dB/cm]	Conf. Interval [dB/cm]
0 nm	3.98	[5.04, 2.92]
140 nm	4.24	[5.31, 3.17]
280 nm	5.62	[6.01, 5.23]

where y_{ij} refers to the intrinsic losses, μ is the overall mean, α_i and $\beta_{j(i)}$ with $i, j = 1, 2, 3$ refer to the three different thicknesses (i) and the three different wafer for each thickness (j), respectively and ε_{ij} is the unexplained residual effect. This model implies that the factor β is nested within factor α because each wafer j can only have one single layer thickness and therefore belongs to a particular level index i of α. Furthermore, we deal with different sorts of effects: while α is a so-called fixed effect, because the levels can be clearly distinguished by the different layer thicknesses, this is not the case for the wafer β, defining it as a random effect. For the latter it is of interest to explain part of the residual variability rather than calculating an effect [21]. So generally, each data value is assumed to be the sum of a common mean, the effect of the different Si_3N_4 layer thicknesses and some random variation, partly explained by the wafer. Note that the outliers shown in Fig. 6b are removed, as usual, from the sample before building the ANOVA model. The null hypothesis that the different Si_3N_4 layer thicknesses have no influence on the damping has now the following form:

$$H_0 : \alpha_1 = \alpha_2 = \alpha_3 \tag{6}$$

The hypothesis test returns the so called p-value [22], which refers to the probability of the effect observed in the given sample under the assumed model and the validity of the null hypothesis. If the returned p-value is smaller than the significance level the null hypothesis is rejected, otherwise if the returned p-value is bigger than the significance level the null hypothesis is accepted. The test of the null hypothesis results in a p-value of $p = 0.0021$ for the Si_3N_4 layer thickness, which is smaller than the chosen significance level of $\alpha_p = 0.05$. Therefore, the null hypothesis of having no influence of layer thickness is rejected. Furthermore, we get estimates of $\sigma_\beta^2 = 0.049$ and $\sigma_\varepsilon^2 = 0.589$ for the variances of the wafer and the residual, respectively, meaning that the wafer explains only a small portion of the variability. Table 1 shows the estimated means and their 95% confidence intervals for the different layer thicknesses.

The lowest estimated intrinsic losses were obtained with the configuration without Si_3N_4 and losses increased with an increasing Si_3N_4 layer thickness. As described above, there is no accurate data for the extinction coefficients of SiO_2 and Si_3N_4 in the mid-infrared range around 4.26 μm. The extinction coefficients for these materials in this range are very low, which makes it difficult to measure on thin films. Altough the extinction coefficients are low, the materials still induce signficiant intrinsic losses. The results stronly suggest that Si_3N_4 has a higher extinction coefficient than SiO_2 in this wavelength range, which leads to the higher damping. This is also in qualitative agreement to the results reported in [17], altough the thin films were prepared using a different method. Finally, Tukey's HSD (honest significant difference) test [23] was used for a pairwise comparison of the influence of the layer thicknesses. Here, the null hypothesis that there is no difference between 0 nm and 140 nm layer thickness was accepted with a p-value of $p = 0.62$. In contrast to that, the null hypothesis was rejected when comparing the intrinsic losses for 0 nm vs. 280 nm and 140 nm vs. 280 nm Si_3N_4 layer thickness, respectively, meaning that there is a significant difference for the intrinsic losses. During the measurements, besides the XY position, also the vertical distance of the fibers to the grating coupler has a crucial impact on the transmitted intensity. Therefore a slightly tilted stage could have an impact on the measurements. In order to investigate if there is a significant effect due to this, the wafer was rotated by 180° for approximately half of the measurements. Without further detail we note that the rotation of the wafer in the measurement setup was also included in the model and tested for significance, but in this case the p-value yielded $p = 0.29$ and the null hypothesis of having no influence due to the rotation of the wafer was accepted.

TABLE 2
Estimated Mean Effect of the Three Different Si_3N_4 Layer Thicknesses and Corresponding 95% Confidence Intervals if the Measured Chip is Included in the ANOVA Model

Si_3N_4	estimate [dB/cm]	conf. interval [dB/cm]
0 nm	3.98	[5.08, 2.87]
140 nm	4.26	[5.37, 3.15]
280 nm	5.62	[6.02, 5.21]

Furthermore, we can add the individual chip number as another random effect $\gamma_{k(j(i))}$, which is nested in the wafer factor $\beta_{j(i)}$, to Eq. 5. This gives very similar results for the estimates of the layer thickness with slightly smaller 95% confidence intervals, summarized in Table 2 and also the significance results of Tukey's HSD test remains unchanged.

However, the extended ANOVA model showed that the chip number within the wafer explains a greater amount of variability than the wafer itself, where the variances are estimated as $\sigma^2_\beta = 0.013$, $\sigma^2_\gamma = 0.173$ and $\sigma^2_\varepsilon = 0.457$ for the wafer, the individual chip number within a wafer and the residual, respectively. Interestingly the chip number showed a larger variability than the change of the mean value for different configurations, which underlines the fact that the measurement of the intrinsic losses with the used approach is challenging. Nevertheless, the ANOVA analysis showed that the substructure configuration affects the intrinsic losses and showed that a substructure using only SiO_2 is favorable yielding an intrinsic damping estimate of 3.98 dB/cm. The results shown in Table 2 are also plotted in Fig. 6b. In literature low loss silicon on insulator waveguides using mid-infrared wavelengths have been reported [24], but these low loss waveguides were achieved using silicon on insulator (SOI) substrates (i.e. waveguides made of single crystaline silicon). The presented poly-Si waveguides that were fabricated using a silicon substrate feature significant intrinsic losses, but for monolothic integration of a full sensor this approach might be necessary.

4.2 Quantitative CO_2 Measurements and Evanescent Field Ratio

In order to test the sensing capability of the strip waveguide, and to estimate the evanescent field ratio, quantitative CO_2 measurements were conducted using a strip waveguide in the form of a meander (also see Fig. 1) with a length of 2 cm. The loop radii of the meander were 25 μm. Using a meander structure allows to incorporate the strip waveguide in an area of less than 1 mm^2 (without coupling structures). The QCL was tuned to a wavelength of $\lambda = 4.23\,\mu$m, which is at the CO_2 absorption line with the highest absorption [25]. It was necessary to conduct the CO_2 measurements at 4.23 μm rather than at 4.26 μm for which the sensor was designed since the QCL emits in a narrow spectral band and the absorption at 4.26 μm is rather low. The sensor was designed for center of the CO_2 absorption band (4.26 μm) since is expected that an integrated infrared source which could be used in the final sensor will rather emit in a wider band that covers the whole CO_2 band. The position of the fibers for in- and out-coupling was adjusted in order to optimize the coupling and achieve a high signal at the detector. Eventually the gas cell (schematic representation is shown in Fig. 4) was flushed using mixtures of N_2/CO_2 and the measured intensity was recorded. The used sequence of CO_2 concentrations was 10000 ppm, 7500 ppm, 5000 ppm, 2500 ppm, 1000 ppm and 500 ppm. As indicated in Fig. 4 the gas entered first the transmission cell in the reference path before it was directed to the measurement cell. The sensor reacts immediately to a change of gas concentration, but due to the time delay that occurs because of the tube paths between the gas mixer and the measurement cell, a rather long time interval of 120 s was used to observe the interaction with each mixture. During the experiment the baseline intensity showed a slight drift, due to a micro drift of the translation stages on which the optical elements were mounted, which led to a continuous change in the alignment. This was taken into account by estimating the baseline by means of a third order polynomial fit through those data points that were obtained when the cell was flushed with nitrogen (which correspond to the baseline).

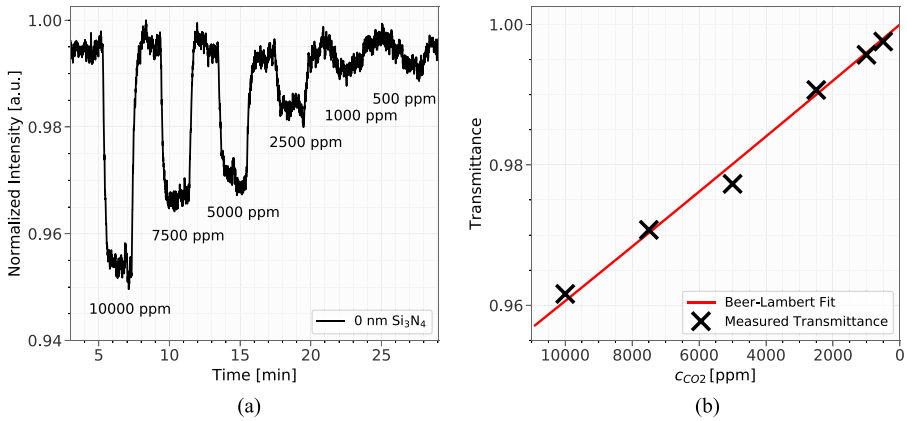

Fig. 7. (a) Quantitative CO_2 measurements for the configuration with 0 nm Si_3N_4. The labels below the data line give the concentration of CO_2 in the gas mixture. (b) Measured transmittance at the six CO_2 concentrations that were used, together with the Beer-Lambert fit using Eq. 7.

The free-beam absorption that occurs between the fiber tips and the waveguide was accounted for as follows. The fibers were placed in close to proximity to each other on one of the launch-pads, while maintaining the same vertical distance to the launchpad that was used during the actual measurements. In this configuration, the radiation which is launched from the first fiber and reflected from the launchpad, directly enters the second fiber. The gas cell was flushed with the sequence described above and the intensities for the different CO_2 concentrations were recorded. The recorded signals from this measurement arise from the absorption in the free-beam path and not from the sensor structure. Therefore, such free-beam contribution is removed from the actual measurement data by dividing the measured data by the free-beam data prior further analysis. A more detailed discription of this procedure can be found in [15]. Fig. 7a shows a representative gas measurement (corrected and normalized), in this case for a substructure configuration of 0 nm Si_3N_4. Qualitatively similar results were obtained with the two remaining configurations.

As visible in the Fig. 7a, it was possible to sense CO_2 concentrations down to 500 ppm. From the measurement results, the transmittance that is associated with each CO_2 concentration was determined from the recorded intensities (after removal of the free-beam contribution). The results are shown in Fig. 7b. The second exponential of the Beer-Lambert law (Eq. 3) which also takes into account the EFR was used to model the sensing behavior of the sensor structure:

$$I = I_0 \cdot e^{-\eta \cdot c \cdot \epsilon \cdot z} \rightarrow T = e^{-\eta \cdot c \cdot \epsilon \cdot z} \tag{7}$$

The parameters are the measured intensity I at a particular CO_2 concentration c, the initial intensity I_0 at $c = 0$, the evanescent field ratio η, the absorption coefficient ϵ and the interaction path z. The measured transmittance T is the ratio of I and I_0. The measured transmittances as a function of the CO_2 concentration c were fitted using Eq. (7) with the evanescent field ratio η as fit parameter. The used parameters were $z = 2$ cm which is the length of the strip waveguide meander and the absorption coefficient $\epsilon = 14.0\,\text{cm}^{-1}$. The absorption coefficient ϵ was determined via quantitative measurements using the reference gas cell (see Fig. 4). The determined absorption coefficient can be understood as an effective absorption coefficient which depends on the absorption spectrum of CO_2 and the characteristics of the IR source (center frequency, spectral shape, spectral bandwidth). The measurements were carried out in analogy to the measurements with the waveguide. The reference cell was flushed with the same sequence of N_2/CO_2 mixtures and the data was fitted using Eq. (7), with $\eta = 1$ since it is a free-beam experiment, with ϵ, the absorption coefficient, as fit parameter. The length of the reference cell z was 10 cm. The evaluated absorption coefficient of $\epsilon = 14.0\,\text{cm}^{-1}$ is rather low if one considers the absorption spectrum of CO_2 [25]. This is caused by two effects, first, the spectral width of the QCL pulses was significantly broader than the CO_2

TABLE 3
Comparison of the Simulated and the Measured Evanescent Field Ratio. The Simulation Results Were Obtained for the Quasi-TE Mode Using the Actual Height of the Waveguides

Height Si_3N_4 [nm]	EFR Simulation [%]	EFR Measurement [%]
0	8.2	14
140	8.8	16
280	8.7	15

absorption line, causing an averaging effect and second, a spurious effect of the ambient CO_2 concentration in the reference beam path which leads to a change of the laser spectrum due to strong absorption at the narrow CO_2 lines.

The least-squares fit of the actual data with the described Beer-Lambert function (Eq. (7)) led to the evanescent field ratios shown in Table 3. The measured evanescent field ratios are compared to simulation results for the quasi-TE mode, where the actual heights of the waveguides were used.

The evanescent field ratios are larger than the values obtained from the simulations. The most probable reason for this discrepancy are the material parameters that were used for the simulations. Overall, it was shown that the waveguides feature a sufficiently high evanescent field ratio and can be used for gas sensing. At this stage, it is hard to judge the repeatability of the sensor itself as the measurement setup also affects the repeatability of the measurement. Nevertheless, the measurement on the waveguide without Si_3N_4 was repeated four times. The measurements showed that the relative standard deviation of the measured transmittances is $< 0.2\,\%$, with the current measurement setup.

5. Conclusion

In this work we presented a numerical and experimental study on sub-wavelength silicon strip waveguides for evanescent gas sensing. The strip waveguides were simulated using a finite element method model and designed for a wavelength of 4.26 μm. The sensor structures were fabricated with standard silicon MEMS technology and are therefore suitable for semiconductor mass production. The two most crucial parameters for an evanescent field sensor structure, the intrinsic losses and the evanescent field ratio were determined. The intrinsic losses were determined for three different configurations of the substructure, where the lowest intrinsic losses were 3.98 dB/cm. Quantitative measurements of CO_2 were conducted down to a concentration of 500 ppm CO_2. Furthermore the the evanescent field ratio was estimated from the CO_2 measurements to be in the range between $\eta = 14$–16%. Future work will target the improvement of the waveguide sensing structures in terms of intrinsic losses and evanescent field ratio and will focus on the integration of a source and a detector in order to fully integrate the presented sensor setup.

Acknowledgment

The authors would like to thank Infineon Technologies Austria AG, especially T. Ostermann for the mask layouts. They also would like to thank M. Ortner for his ongoing support regarding the Python programming language.

References

[1] N. Barsan, D. Koziej, and U. Weimar, "Metal oxide-based gas sensor research: How to?" *Sensors Actuators B, Chem.*, vol. 121, no. 1, pp. 18–35, 2007.
[2] A. Ghatak and K. Thyagarajan, *An Introduction to Fiber Optics*. Cambridge, U.K.: Cambridge Univ. Press, 1998.
[3] M. C. Teich and B. Saleh, *Fundamentals of Photonics*. Toronto, ON, Canada: Wiley, vol. 3, 1991.
[4] K. Okamoto, *Fundamentals of Optical Waveguides*. Orlando, FL, USA: Academic, 2010.
[5] R. Orghici, U. Willer, M. Gierszewska, S. Waldvogel, and W. Schade, "Fiber optic evanescent field sensor for detection of explosives and CO_2 dissolved in water," *Appl. Phys. B, Lasers Opt.*, vol. 90, no. 2, pp. 355–360, 2008.

[6] V. M. Lavchiev and B. Jakoby, "Photonics in the mid-infrared: Challenges in single-chip integration and absorption sensing," *IEEE J. Sel. Topics Quantum Electron.*, vol. 23, no. 2, pp. 1–12, Mar./Apr. 2017.
[7] V. Lavchiev, B. Jakoby, U. Hedenig, T. Grille, J. Kirkbride, and G. Ritchie, "M-line spectroscopy on mid-infrared Si photonic crystals for fluid sensing and chemical imaging," *Opt. Exp.*, vol. 24, no. 1, pp. 262–271, 2016.
[8] Y. Huang, S. K. Kalyoncu, Q. Zhao, R. Torun, and O. Boyraz, "Silicon-on-sapphire waveguides design for mid-IR evanescent field absorption gas sensors," *Opt. Commun.*, vol. 313, pp. 186–194, 2014.
[9] R. Jannesari, C. Ranacher, C. Consani, T. Grille, and B. Jakoby, "Sensitivity optimization of a photonic crystal ring resonator for gas sensing applications," *Sensors Actuators A, Phys.*, vol. 264, pp. 347–351, 2017.
[10] R. Siebert and J. Müller, "Infrared integrated optical evanescent field sensor for gas analysis: Part I: System design," *Sensors Actuators A, Phys.*, vol. 119, no. 1, pp. 138–149, 2005.
[11] R. Siebert and J. Müller, "Infrared integrated optical evanescent field sensor for gas analysis: Part II. Fabrication," *Sensors Actuators A, Phys.*, vol. 119, no. 2, pp. 584–592, 2005.
[12] C. Ranacher *et al.*, "Spectroscopic gas sensing using a silicon slab waveguide," *Procedia Eng.*, vol. 168, pp. 1265–1269, 2016.
[13] X. C. Tong, *Advanced Materials for Integrated Optical Waveguides*. Berlin, Germany: Springer, 2014.
[14] C. Ranacher, C. Consani, U. Hedenig, T. Grille, V. Lavchiev, and B. Jakoby, "A photonic silicon waveguide gas sensor using evanescent-wave absorption," in *Proc. SENSORS*, 2016, pp. 1–3.
[15] C. Ranacher *et al.*, "Mid-infrared absorption gas sensing using a silicon strip waveguide," *Sensors Actuators A, Phys.*, vol. 277, pp. 117–123, 2018.
[16] D. F. Edwards and E. Ochoa, "Infrared refractive index of silicon," *Appl. Opt.*, vol. 19, no. 24, pp. 4130–4131, 1980.
[17] J. Kischkat *et al.*, "Mid-infrared optical properties of thin films of aluminum oxide, titanium dioxide, silicon dioxide, aluminum nitride, and silicon nitride," *Appl. Opt.*, vol. 51, no. 28, pp. 6789–6798, 2012.
[18] K. Luke, Y. Okawachi, M. R. Lamont, A. L. Gaeta, and M. Lipson, "Broadband mid-infrared frequency comb generation in a Si_3N_4 microresonator," *Opt. Letters*, vol. 40, no. 21, pp. 4823–4826, 2015.
[19] S. A. Miller *et al.*, "Low-loss silicon platform for broadband mid-infrared photonics," *Optica*, vol. 4, no. 7, pp. 707–712, 2017.
[20] D. C. Montgomery, *Design and Analysis of Experiments*. Hoboken, NJ, USA: Wiley, 2017.
[21] T. Snijders and R. J. Bosker, *Multilevel Analysis: An Introduction to Basic and Advanced Multilevel Modeling,* 2nd ed. Newbury Park, CA, USA: Sage, 2012.
[22] R. L. Wasserstein and N. A. Lazar, "The ASA's statement on p-values: Context, process, and purpose," *Amer. Statistician*, vol. 70, pp. 129–133, 2016.
[23] J. W. Tukey, "Comparing individual means in the analysis of variance," *Biometrics*, vol. 5, pp. 99–114, 1949.
[24] H. Lin *et al.*, "Mid-infrared integrated photonics on silicon: A perspective," *Nanophotonics*, vol. 7, no. 2, pp. 393–420.
[25] L. S. Rothman *et al.*, "The HITRAN2012 Molecular Spectroscopic Database," *J. Quant. Spectrosc. Radiat. Transfer*, vol. 130, pp. 4–50, 2013.